



Power Electronic Systems
Laboratory

© 2015 IEEE

Proceedings of the IEEE Energy Conversion Congress & Expo (ECCE USA 2015), Montreal, Canada, September 20-24, 2015

Loss Investigation of Slotless Bearingless Disk Drives

D. Steinert,
I. Kovacevic-Badstübner,
T. Nussbaumer,
J. W. Kolar

This material is published in order to provide access to research results of the Power Electronic Systems Laboratory / D-ITET / ETH Zurich. Internal or personal use of this material is permitted. However, permission to reprint/republish this material for advertising or promotional purposes or for creating new collective works for resale or redistribution must be obtained from the copyright holder. By choosing to view this document, you agree to all provisions of the copyright laws protecting it.



Eidgenössische Technische Hochschule Zürich
Swiss Federal Institute of Technology Zurich

Loss Investigation of Slotless Bearingless Disk Drives

Daniel Steinert*, Ivana Kovacevic-Badstübner*, Thomas Nussbaumer†, Johann W. Kolar*

*Power Electronic Systems Laboratory, ETH Zurich, Switzerland, Email: steinert@lem.ee.ethz.ch

†Levitronix GmbH, 8005 Zurich, Switzerland, Email: nussbaumer@levitronix.ch

Abstract—Losses are often a limiting factor for the application of bearingless motors, especially at high rotational speeds. In this paper the loss mechanisms in slotless bearingless disk drives with toroidal windings are identified and analyzed. Although the slotless topology already features comparably low losses, a detailed comprehensive analysis of the loss portion enables a further reduction of these losses. To obtain the loss composition, computationally efficient simulation and calculation methods as well as simple measurement methods are presented for each loss component, considering iron losses, eddy current losses in the coils, PWM induced losses, copper losses, windage losses, and inverter losses. This allows for optimization of the motor geometry towards minimized losses. The analysis results are compared with loss measurements of four different motors with different rotor sizes, pole pair numbers, and coil configurations.

Keywords—iron loss, loss composition, bearingless slice motor, magnetic levitation.

I. INTRODUCTION

In a bearingless motor — also called self-bearing motor — the rotor is levitated magnetically in the middle of the stator without any mechanical contact, where motor and bearing functionality are integrated into one magnetic circuit [1]. Due to the absence of lubrication and abrasion, this motors can be used, for example, in vacuum applications, high speed applications [2], [3], or in applications with high demands on purity or chemical resistance, as they exist in pumps and mixers [4]–[6]. However, bearingless motors often have high electromagnetic losses – especially at high speeds – which is due to the big air gap and the high magnetic fields needed for the magnetic bearing. Especially at the teeth in most of the topologies, the high spatial field harmonics induce high eddy current and hysteresis losses in the stator iron and eddy current losses in the conductive parts of the rotor. This is one of the most critical drawbacks of bearingless motors, as it limits the achievable power densities and rotational speeds needed for many applications. Therefore, the topologies investigated in this paper consist of a slotless ring-shaped stator, as they are presented in [7]–[9], which results in reduced losses compared to conventional-type bearingless motors.

To further optimize and reduce the losses, a detailed and comprehensive analysis of the loss portions of this bearingless motor type is conducted in this paper. With particular consideration of the motor size and pole pair number, this also enables the prediction of the power consumption for various slotless motors. The identified loss mechanisms are the iron losses in the stator iron, eddy current losses in the coils, harmonic

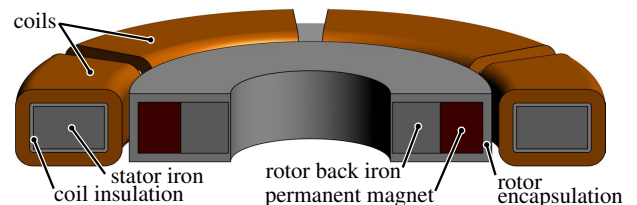


Fig. 1: Basic setup of a slotless bearingless disk drive. The coils are wound toroidally around a ring-shaped stator iron. The rotor consists of permanent magnets mounted on a back iron and is encapsulated by a stainless steel shell to withstand high circumferential speeds.

losses induced by the current ripple, windage losses at the rotor surface, and losses in the inverter.

In the Section II, the concerning slotless topologies are explained and the analyzed prototypes are presented. The main loss mechanisms are explained in Section III, and estimation and measurement methods are given. In Section IV, the loss composition is discussed using the results of the four prototypes. Measurements are shown and compared to the theoretical analysis to prove the validity of the analysis.

II. THE SLOTLESS BEARINGLESS DISK DRIVE

The considered slotless topologies consist of a ring-shaped stator, which holds toroidally wound coils for torque and force generation. Figure 1 shows a cross-section of the motor. The rotor is also ring-shaped and consists of permanent magnets mounted on a back iron. The rotor is passively stable against axial displacements and tilting, as the permanent magnets produce reluctance forces towards the stator iron. In radial direction, the rotor has to be stabilized actively by the stator coils. The magnetic field of the rotor penetrates the coils and produces Lorentz- and reluctance forces in conjunction with the coil currents. With appropriate current commands, bearing force and drive torque can be controlled independently. In [7] the operating principle of this motor type is explained in more detail.

In this paper, the losses of three different motor topologies [10] are considered, which differ in rotor pole pair number and winding configuration. The six-coil topology is designed for a diametrically magnetized rotor with one pole pair as shown in Fig. 2(a). It is a combined coil concept, which means that torque and bearing force are generated simultaneously with the same set of coils. This topology is well suited when low losses and high speeds are required. The 6-coil stator can also

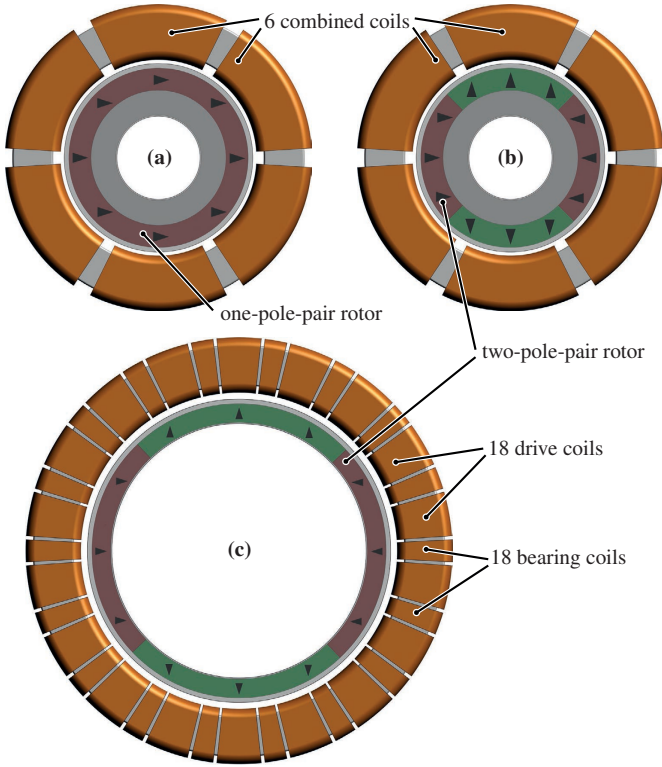


Fig. 2: Overview of the analyzed winding configurations: (a) The 6-coil topology with one-pole-pair rotor is used by the prototypes S10.P1 and S10h.P1. (b) The 6-coil topology can also be operated with a two-pole pair rotor as shown with the prototype S10.P2, but it features very low bearing performance. (c) The 36-coil topology is the best for two-pole-pair rotors and features high bearing stiffness. It is used in the prototype S16.P2.

be used with a two-pole-pair rotor, as shown in Fig. 2(b). As this configuration features low bearing performance, it is not recommended for practical application, but it is used in this paper to directly compare the losses of a one- and a two-pole-pair rotor. The third topology has 36 coils and uses 18 coils for the drive and 18 coils for levitating a two-pole-pair rotor (cf. Fig. 2(c)). This topology features high passive and active bearing stiffness and can be used in applications with high mechanical loads.

For each topology, a prototype was built to measure the losses and compare them to the analysis results, which are shown later. The stator S10 has six coils and a rotor with 10 cm outer diameter. It can be used with a one- and a two-pole-pair rotor and will be referred to as S10.P1 and S10.P2. A variation of this stator, called S10h, features a higher stator and thinner magnets. It is used only with a one-pole-pair rotor and will be referred to as S10h.P1. For the 36-coil topology, a prototype is available that uses only two-pole-pair rotors with 16 cm outer diameter. This prototype is called S16.P2, according to its rotor diameter and pole-pair number.

The details for all four prototypes are summarized in Table I. As different pole-pair numbers, different winding topologies, as well as different geometries are available, the theoretical loss analysis can be validated comprehensively. The prototypes S10.P1 and S10.P2 allow the direct comparison of the losses for different pole-pair numbers without changing the

TABLE I: Parameters of the tested prototypes

	S10.P1	S10.P2	S10h.P1	S16.P2
rotor pole pairs	1	2	1	2
number of coils	6	6	6	2x18
coil type	combined	combined	combined	separated
rotor diameter	10 cm	10 cm	10 cm	16 cm
motor height	2.5 cm	2.5 cm	3.5 cm	2.5 cm

TABLE II: Overview of analyzed loss types and main dependency for a given motor

loss type	caused by	mainly dependent on
iron loss	P_{Fe}	rotor field
copper eddy current loss	$P_{Cu,Ed}$	rotor field
resistive copper loss	$P_{Cu,R}$	coil current
harmonic loss	P_{harm}	current ripple
windage loss	P_{wind}	air friction
controller loss	P_{ctrl}	power electr.

geometry or winding topology.

Despite the differences in the prototypes, the loss mechanisms, which will be analyzed in the following chapter, are the same in all prototypes.

III. LOSS MECHANISMS

The total losses of the system

$$P_{tot} = P_{ctrl} + P_{Fe} + P_{Cu,R} + P_{Cu,Ed} + P_{harm} + P_{wind} \quad (1)$$

consist of controller losses P_{ctrl} , iron losses P_{Fe} in the stator, resistive copper losses $P_{Cu,R}$, eddy current losses $P_{Cu,Ed}$ in the coils induced by the rotor permanent magnets, high frequency harmonic losses P_{harm} induced by the PWM switching frequency, as well as windage losses P_{wind} at the rotor surface. Table II gives an overview of all analyzed loss types, their main cause, as well as the main dependency for a given motor.

A. Stator Iron Losses

In the stator iron, which guides the magnetic flux of the rotor magnets, losses occur when the rotor is spinning. According to the Steinmetz model, these iron losses

$$P_{Fe} = P_{Fe,H_y} + P_{Fe,Ed} \quad (2)$$

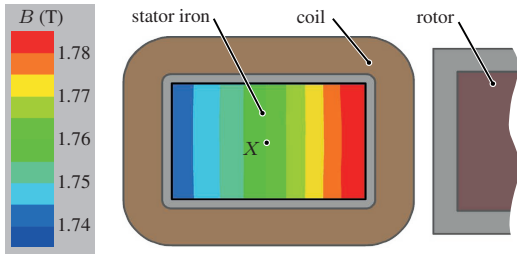
can be divided into hysteresis losses P_{Fe,H_y} , and eddy current losses $P_{Fe,Ed}$ [11]. The hysteresis losses

$$P_{Fe,H_y} = c_{H_y} m_{Fe} f_{el} \hat{B}^{1.6} \quad (3)$$

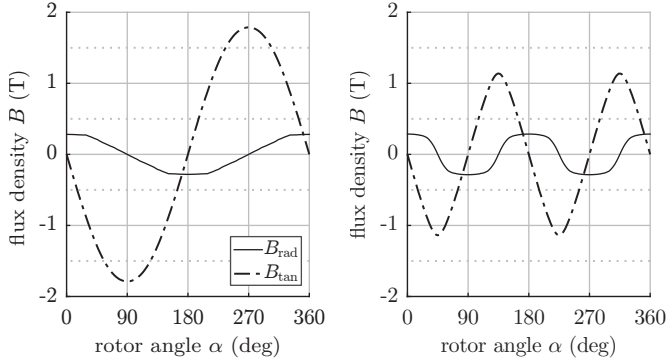
are estimated by the peak flux density \hat{B} in the stator, the electric frequency f_{el} , and the mass m_{Fe} of the stator. As these losses result from the hysteresis in the BH-curve of the stator material, they are not influenced by higher harmonics of the magnetic field, as long as the direction of the waveform is not reversed [12]. Contrarily, for the eddy currents

$$P_{Fe,Ed} = c_{Ed} m_{Fe} t_{Fe}^2 \sum_{i=1}^j f_{el,i}^2 \left(\hat{B}_{tan,i}^{2.3} + \hat{B}_{rad,i}^{2.3} \right) \quad (4)$$

each harmonic waveform i of the radial and tangential field \hat{B}_{tan} and \hat{B}_{rad} contributes to the losses.



(a) 3D simulation with rotor P1



(b) 2D sim. with rotor P1

(c) 2D sim. with rotor P2

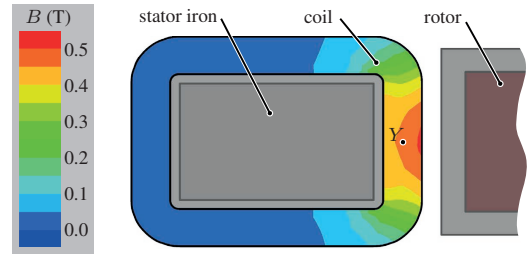
Fig. 3: (a) 3D simulation of the flux density distribution in the stator with rotor P1 at rotor position $\alpha = 270^\circ$. (b) 2D Simulation result of flux density in the center of the stator iron [position X in (a)] for one revolution of the rotor P1 and (c) the rotor P2. It can be observed that the tangential flux density is dominant and sinusoidal. For a P2 rotor, the peak flux density is lower than for a P1 rotor.

The coefficients c_{Hy} and c_{Ed} have to be identified from measurements or can be obtained from the manufacturer. For the material M270-35A, which was used in the prototypes, loss measurements from the manufacturer [13] were used to calculate the coefficients by the least squares method. The determined coefficients are given in Table III.

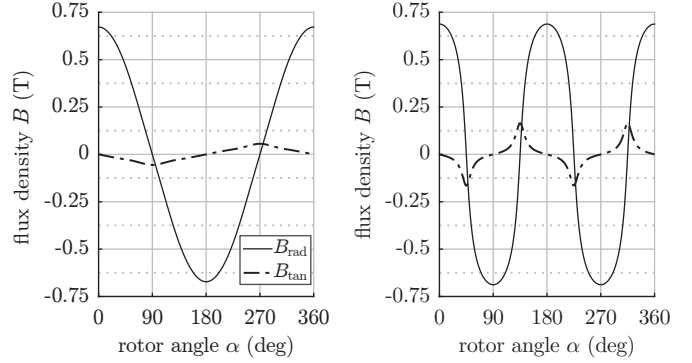
The peak flux density can be simulated in a magnetostatic 3D FEM simulation. Figure 3(a) shows the flux density in the stator at the position between two rotor poles, which is where the peak flux density occurs. The flux density is only slightly higher at the stator side facing the rotor. As it is almost homogeneously distributed along the cross-section, its mean value can be used to calculate the iron losses. The shape of the field along the stator perimeter is simulated by 2D FEM in the middle of the stator, which is shown in Figs. 3(b) and (c) for one revolution of a one- and a two-pole-pair rotor. This is used to determine the harmonics for Eq. (4). In the direct comparison of the one- and two-pole-pair rotor it can be seen that the peak flux density for the two-pole-pair rotor is significantly lower. The shape of the field is still nearly sinusoidal, such that harmonics can be neglected, if the analysis is intended to be simplified.

TABLE III: Iron loss parameters identified for M270-35A

Parameter	Symbol	Value	Unit
Hysteresis coefficient	c_{Hy}	0.02	W/(kg Hz T ^{1.6})
Eddy current coefficient	c_{Ed}	500	W/(kg m ² Hz ² T ^{2.3})



(a) 3D simulation with rotor P1



(b) 2D sim. with rotor P1

(c) 2D sim. with rotor P2

Fig. 4: (a) 3D simulation of the flux density distribution in the coil with rotor P1 at position $\alpha = 0^\circ$. The flux from the permanent magnet radially penetrates the coils in the air gap. The highest flux density occurs in the center of the coil and decreases towards the top and bottom. (b) 2D Simulation result of the flux density in the center of the coil [position Y in (a)] for one revolution of the rotor P1 and (c) rotor P2. It can be observed that the radial flux density is dominant. The peak flux density is nearly the same for both rotors, but it is less sinusoidal for the two-pole-pair rotor.

B. Eddy Current Copper Losses

In contrast to classical motors with distinct slots, the copper wires of the slotless motor topology are directly penetrated by the magnetic field of the rotor, as parts of the coil wires are inside the magnetic gap. Consequently, eddy currents are induced in the wires when the rotor is spinning. Figure 4(a) shows the B-field in the coil in front of a rotor pole as simulated by 3D FEM. It is observed that the magnetic flux vector can be decomposed into two components in the cylindrical coordinate system: the tangential component, B_{tan} and the radial component B_{rad} . In the Figures 4(b) and (c) the radial and tangential flux densities are plotted for a one- and a two-pole-pair rotor, respectively, as simulated in 2D FEM. Moreover, with the rotation of the rotor, the flux density – especially with the two-pole-pair rotor – is not exactly sinusoidal but comprises higher order harmonics.

As the copper eddy current losses originate in the same way as the so called proximity losses from an external magnetic field penetrating a round copper wire, the same calculation methods can be used. As shown in [14], these losses are calculated by

$$P_{Cu,Ed} = wN \sum_{i=1}^{\infty} \int_L \frac{\pi^3 d^4 f_{el,i}^2 \hat{B}_i^2}{32\rho_{Cu}} dl \quad (5)$$

where N is the number coils, w is the number of turns per coil, d is the wire diameter, ρ_{Cu} is the resistivity of copper,

\hat{B}_i is the amplitude of the i -th harmonic of the B-field with the frequency f_{el} , and $f_{el,i}(= i \cdot f_{el})$ is the i -th frequency harmonic. The losses are integrated along the complete wire length L of each turn. In the next step, (5) is simplified using the root-mean-square (rms) of the magnetic flux over the cross-sectional area of the stator, $\hat{B}_{rms,i}$,

$$P_{Cu,Ed} = \frac{\pi^3}{32\rho_{Cu}} wNd^4 f_{el}^2 \bar{L} \sum_{i=1}^{\infty} \left(i^2 \hat{B}_{rms,i}^2 \right) \quad (6)$$

where \bar{L} is the mean wire length per turn as calculated using

$$\bar{L} = \frac{A_{coil}}{t_{coil}}, \quad (7)$$

where A_{coil} and t_{coil} are the cross-sectional coil area and coil thickness, respectively. The rms value of the magnetic flux is obtained by integrating the peak flux density over the cross-sectional area of the stator using

$$\hat{B}_{rms,i} = \sqrt{\frac{1}{A_{coil}} \int_{A_{coil}} \hat{B}_i^2 dA}. \quad (8)$$

If it is assumed that the shape of the magnetic field does not change over the cross-sectional area of the coil, i.e., $\hat{B}_{tan,i}/\hat{B}_{rms}$ and $\hat{B}_{rad,i}/\hat{B}_{rms}$ are constant for every point of A_{coil} , where \hat{B}_{rms} is the rms value of total B-field calculated using 3D FEM simulation, then (6) can be simplified by means of a distortion factor ξ , as,

$$P_{Cu,Ed} = \frac{\pi^3}{32\rho_{Cu}} wNd^4 f_{el}^2 \bar{L} \left(\hat{B}_{rms} \cdot \xi \right)^2, \quad (9)$$

$$\xi = \frac{1}{\hat{B}_{rms,2D}} \sqrt{\sum_{i=1}^{\infty} \left(\hat{B}_{tan,2D,i}^2 + \hat{B}_{rad,2D,i}^2 \right) \cdot i^2}, \quad (10)$$

where $\hat{B}_{rms,2D}$, $\hat{B}_{rad,2D,i}$ and $\hat{B}_{tan,2D,i}$ are the B-field components as calculated from a 2D FEM simulation.

The reason for the 2D-to-3D scaling is that 2D and 3D FEM simulations return different magnitudes but the same shape of the B-field. As any axial stray flux and the axial dimension is neglected for 2D FEM assuming the same depth of all modeled objects, a 3D FEM simulation is necessary for a more accurate calculation of the B-field. However, 3D FEM simulation of the tangential and radial B-field components and their higher harmonics with high precision requires longer computational time, and thus, these components are typically obtained from 2D FEM analysis in common engineering practice.

The distortion factor ξ , which can completely be simulated by 2D FEM, only contains information about the shape of the field. It indicates the influence of the harmonics as well as the radial and tangential field components on the losses, compared to a purely sinusoidal and alternating field. In Table IV, the distortion factors for all four evaluated prototypes are given. It is shown that for both one-pole-pair rotors the distortion factor is identical to one ($\xi = 1$) and, therefore, has no influence. However, as the harmonics and the radial field components increase with a two-pole-pair rotor, these prototypes show a

TABLE IV: Distortion factors determined for all prototypes

motor	pole-pair number p	distortion factor ξ
S10.P1	1	1.00
S10h.P1	1	1.00
S10.P2	2	1.36
S16.P2	2	2.15

significantly higher distortion factor. Therefore, the shape of the field has to be considered for loss calculation of motors with multiple pole-pairs, but can be neglected for one-pole-pair machines.

The eddy current losses in the coils are dependent on the rotational speed of the motor, but independent of the load torque. The use of litz wire instead of solid wire would almost eliminate this loss component, however, the load dependent resistive copper losses would increase due to the higher resistance of litz wire. Consequently, the optimal wire diameter depends on the desired rotational speed and load torque and can be optimized for the respective application.

C. Resistive Copper Losses

Due to the bearing and drive currents, load dependent resistive copper losses occur in the coils. As the bearing currents are minimized by the applied control algorithm, only the drive currents have to be considered. The copper losses

$$P_{Cu,R} = mRI_D^2 \quad (11)$$

in the m drive phases with the resistance R are calculated using the drive current

$$I_D = \frac{T}{k_D} = \frac{1}{2\pi nk_D} (P_{mech} + P_{Fe} + P_{Cu,Ed} + P_{wind}), \quad (12)$$

which originates from the load torque T on the rotor and the drive constant k_D . The torque on the rotor results from the mechanical output power P_{mech} , the rotational speed n , and the losses P_{Fe} , $P_{Cu,Ed}$, and P_{wind} .

D. Harmonic Losses

Another cause of losses in a slotless bearingless motor is the ripple of the coil currents, which generates high frequency magnetic fields. These fields penetrate the stator as well as the rotor and induce eddy current losses in the coils, the stator iron, and the conductive shell of the rotor. The resulting losses are referred to as harmonic losses P_{harm} in this paper.

The current ripple originates from the PWM-controlled pulsating voltage drop across the motor inductance. The high flux density in the air gap, which is necessary to achieve high passive stiffness in a disk-type motor, results in a high flux linkage in the coils. This requires a low number of winding turns to achieve the maximum rotational speed for a given maximum inverter voltage. Therefore, the inductances are especially low in the considered high-speed bearingless disk-type motor topology, which results in substantial current ripples compared to classical low speed motors.

Due to the high frequency of the current ripple, the skin depth is below the dimensions of the motor, and the eddy current reaction field has to be taken into account. Schwager

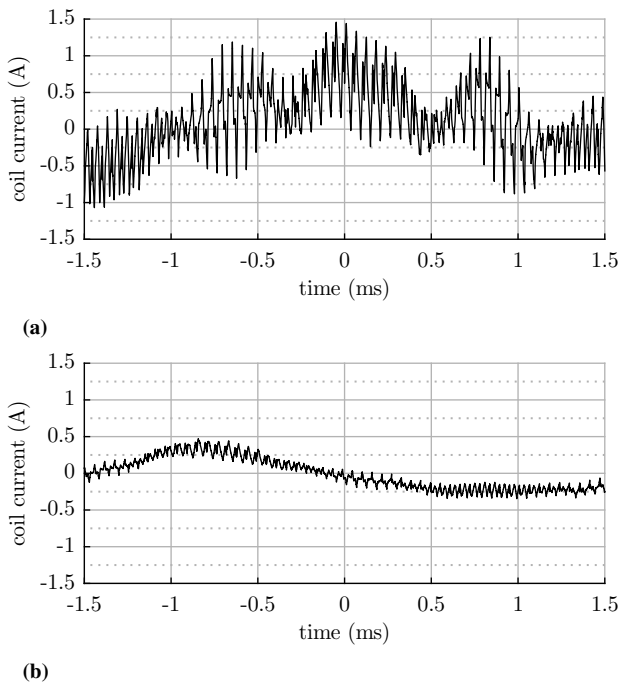


Fig. 5: Measured coil current (a) without and (b) with filter inductance of prototype S10.P1 at 20000 r/min without load. By using a filter the input power of the motor was lowered by 24 W compared to the measurement without filter.

et. al. [15] analytically calculated the field resulting from the PWM ripple in a permanent magnet synchronous machine (PMSM). With this, the eddy current losses in the stator and the rotor were calculated in 2D. Unfortunately, 2D methods are not reliable for disk-type motors due to the axial stray flux. Yamazaki and Abe [16] present a method for simulating the losses resulting from the PWM in a PMSM by transient 3D FEM simulation. The presented results fit well with the presented measurement results, but the reported computational effort of more than 50 days and the complexity of the simulation exceed the scope of this analysis. Bradley et. al. [17] present a method for measuring the losses for existing prototypes. A sinusoidal voltage with variable frequency is superimposed on the supply voltage of the machine and its influence on the losses is measured. The loss portion for each harmonic component of the actual supply voltage is then calculated with the results from the experiment.

In this paper, a similar experimental approach is chosen. For each prototype, the losses are measured with an additional filter inductance that is put in series with each supply phase. This filter inductance was multiple times higher than the motor inductance itself. In Fig. 5 the measured input current is shown without and with filter during operation at maximum speed. As the current ripple is significantly reduced by the filter, it is supposed that the harmonic losses are negligible in this case. Then, the harmonic loss in normal operation can be calculated by the difference of the losses with and without filter.

E. Inverter Losses

The inverter losses

$$P_{\text{ctrl}} = P_{\text{ctrl},0} + \chi_{\text{ctrl}} \cdot P_{\text{mot}} \quad (13)$$

can be separated into a constant part $P_{\text{ctrl},0}$ representing the load independent power consumption of the controller electronics, and a load dependent part, which consists of switching and conduction losses and depends on the electric output power P_{mot} . Measurements for the utilized 2 kW inverter show a constant power consumption of $P_{\text{ctrl},0} = 22 \text{ W}$ and load dependent losses of about $\chi_{\text{ctrl}} = 8\%$ of the output power. The measurement was conducted under normal motor operation measuring the input power at the inverter with a wattmeter and the output power with an oscilloscope.

F. Windage Losses

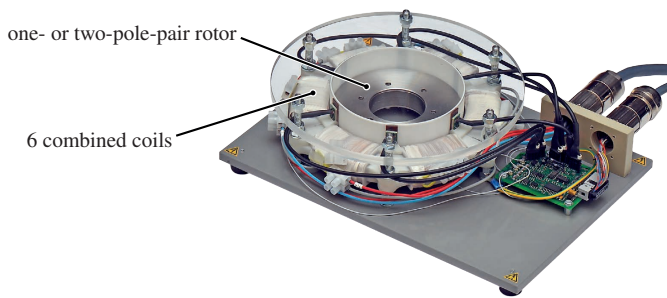
In addition to the electromagnetic losses, the drag acting on the rotor surface generates speed dependent losses. For the estimation of these air friction losses, various methods exist in the literature. Borisavljevic [18] presents different models for the friction at disks and cylinders rotating inside an enclosure. Also the model of Bilgen and Bolous [19] is known to calculate the friction at the outer surface of a rotor. However, these models do not take into account the drag torque at the top, bottom and inner surface of the rotor. Another model for disk-type rotors considering also the top and bottom surface is presented by Mitterhofer [20]. This model can be adapted to ring-shaped rotors by subtracting the drag torque that would act on the inner part of the ring. However, no model was found that showed satisfying agreement with the measurements conducted for the prototypes.

Therefore, only the measurements of the windage losses are considered in this paper. For this purpose, the rotor chamber of each prototype was sealed and evacuated with a vacuum pump, leaving a residual pressure of just 0.05 bar. The difference of the measured motor input power at operation in vacuum and under normal conditions yields the windage loss.

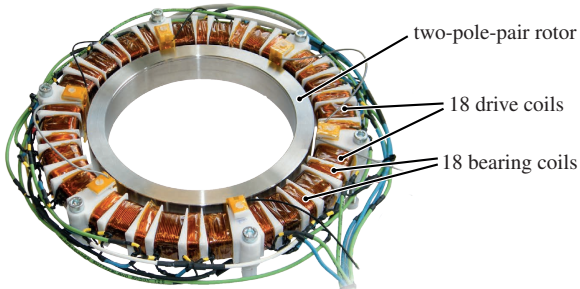
IV. EXPERIMENTAL RESULTS

As mentioned before, the total losses were measured on four different prototypes to confirm the analytical loss investigation. Photographs of the prototypes S10.P1/2 and S16.P2 are shown in Fig. 6, and the geometrical details are given in Table I.

The losses of all prototypes were measured with a wattmeter at the input of the inverter. Additionally, the windage losses were measured under vacuum operation for the prototypes S10.P1 and S16.P2. For the prototype S10.P2 the windage losses are identical to the ones of the S10.P1 as the geometry is the same. For the prototype S10h.P1, the windage losses were estimated from the measurement results taken with the S10.P1 using the total rotor surface. As the geometry is similar, this is a good approximation. The harmonic losses were measured at the prototypes S10.P1, S10h.P2 and S16.P2 by using the filter inductances. For the prototype S10.P2 it is assumed, that the harmonic losses are similar to the S10.P1 due to the same geometry. The influence of the pole-pair number is neglected here.



(a) prototype S10.P1/P2



(b) prototype S16.P2

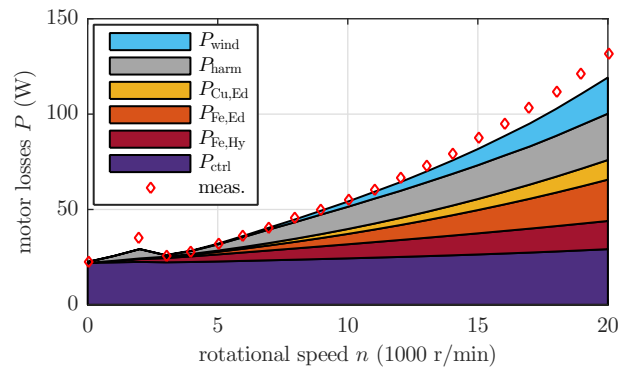
Fig. 6: Test setups of the slotless bearingless disk drive prototypes. (a) Prototype S10 with six coils and a rotor with 10 cm outer diameter. The motor S10 can be operated with rotors with one (S10.P1) and two pole-pairs (S10.P2). (b) Prototype S16.P2 with an outer rotor diameter of 16 cm is operated only with a rotor with two pole-pairs. The prototype S10h looks similar to the prototype S10 and is not shown here.

The results for all prototypes are shown in Fig. 7. The measurement of the total losses are compared to the composition of the particular losses (area plots). It can be observed that for all four machines the measurement results fit well with the analysis results. Only the prototype S10.P2 shows higher losses than expected, which can be attributed to the harmonic losses, which were not measured but just taken from the prototype S10.P1.

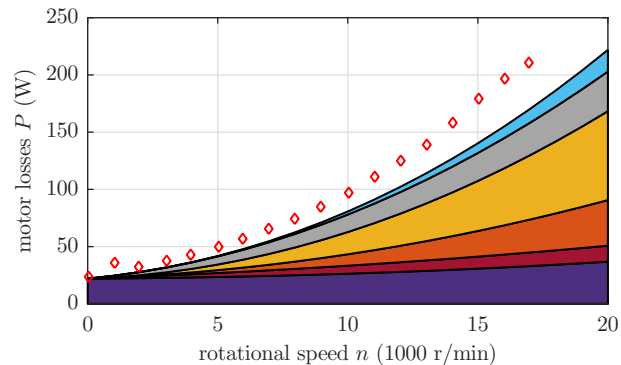
All machines show a significant portion of harmonic losses. This is, as explained, due to the low inductance of the coils in this slotless topology. Especially in the prototype S10h.P1 harmonic losses are high. This is due to the lower winding number as compared to the S10.P1, which decreases the inductance and increases the harmonic losses, as well as due to the bigger iron volume. With an output current filter or with improved inverter technology – for example with multi level inverters or higher switching frequency – these losses can be reduced.

The eddy current losses in the coils are small in the one-pole-pair machines, but quite significant for the two-pole-pair machines. This is due to the higher electrical frequency and the distortion of the field. With litz wires, these losses can be nearly eliminated, but the load dependent copper losses would increase due to the higher resistance (for a certain given copper space).

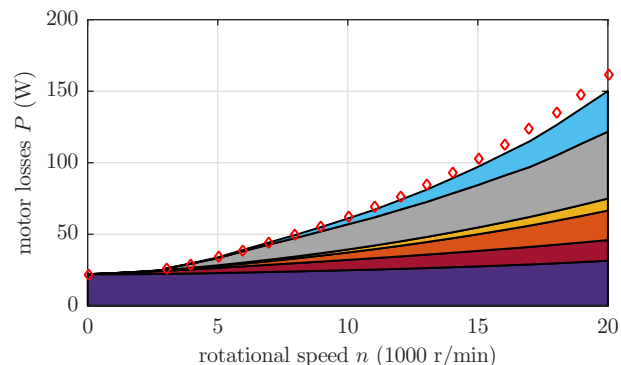
These copper losses are not shown in the no load measurements, as they are always below 2 W in this case. However, under load operation they will get more important, as they increase quadratically with the output power, as shown in Eq. (11).



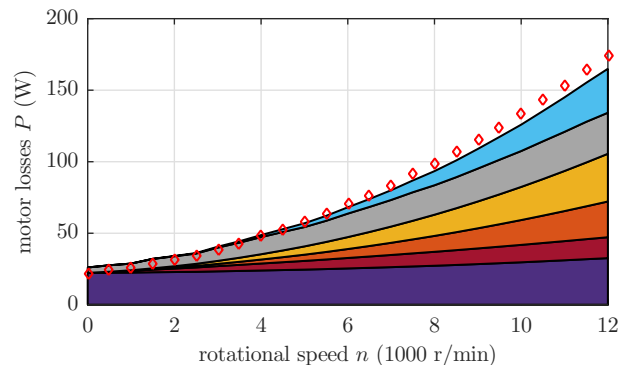
(a) prototype S10.P1



(b) prototype S10.P2



(c) prototype S10h.P1



(d) prototype S16.P2

Fig. 7: Measured losses and predicted loss parts for all four evaluated prototypes. The windage losses and harmonic losses are measured (except for S10.p2). The other loss parts are calculated. The resistive copper losses are not shown in the diagrams, as they are too small to be visible here.

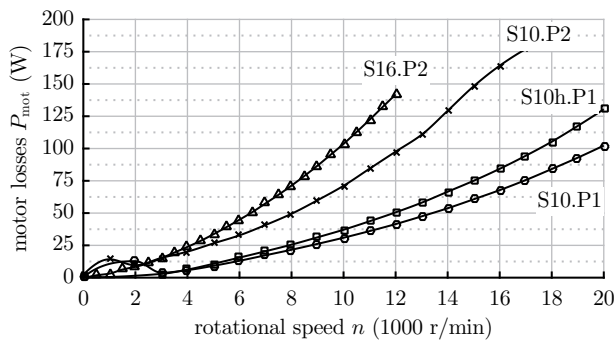


Fig. 8: Total motor losses (without inverter losses) of all prototypes. The increase of losses from S10.P1 to S10.P2 is due to the pole-pair number increase from one to two. The highest losses occur in prototype S16.P2 due to size and pole-pair number.

The portion of the iron losses is similar for all machines. At high speeds, the eddy current losses in the stator iron exceed the hysteresis losses, which justifies the usage of sheeted stator material.

Figure 8 shows the direct comparison of the measured total motor losses. For better comparison, the inverter losses have been subtracted. Prototype S10.P1 exhibits the lowest overall losses, as it has the lowest pole-pair number and the smallest size. The losses of prototype S10h.P1 are slightly higher due to its bigger iron volume and lower winding number. The big increase in motor loss from one- to two-pole pairs can be seen for prototype S10.P2. Prototype S16.P2 exhibits a further increase, as it is also increased in size.

V. CONCLUSIONS

A comprehensive loss analysis was conducted for the slotless bearingless disk drive. Various loss mechanisms are identified and models or measurement methods are presented to quantify each loss portion. The measurement results confirm the theoretical results and show that the analysis is complete. The analysis is valid for different geometries, different pole-pair numbers, and different winding configurations. For the harmonic losses and windage losses only measurement methods were presented. Further research could be conducted to find models, which enable the reliable estimation of these losses without measurements on existing prototypes.

Besides the iron and windage losses, harmonic losses and eddy current copper losses have been identified to be of importance in this type of motors. As each loss mechanism is based on different motor properties, an optimization for specific applications is now possible with the presented loss analysis. It depends on the application, whether the loss reduction e. g. obtained by an output filter to reduce the harmonic losses or by litz wire is worth the additional cost or not. Moreover, as the amount of iron losses is lower than it might be expected, costs can be reduced by using cheaper stator material, if the additional losses are allowable for the intended application.

REFERENCES

- [1] X. Sun, L. Chen, and Z. Yang, "Overview of bearingless permanent-magnet synchronous motors," *IEEE Trans. Ind. Electron.*, vol. 60, pp. 5528–5538, Dec. 2013.
- [2] C. Zwyssig, T. Baumgartner, and J. Kolar, "High-speed magnetically levitated reaction wheel demonstrator," in *Power Electronics Conference (IPEC-Hiroshima 2014 - ECCE-ASIA), 2014 International*, pp. 1707–1714, May 2014.
- [3] T. Baumgartner, R. Burkart, and J. Kolar, "Analysis and design of a 300-w 500 000-r/min slotless self-bearing permanent-magnet motor," *IEEE Trans. Ind. Electron.*, vol. 61, pp. 4326–4336, Aug. 2014.
- [4] J. Asama, D. Kanehara, T. Oiwa, and A. Chiba, "Development of a compact centrifugal pump with a two-axis actively positioned consequent-pole bearingless motor," *IEEE Trans. Ind. Appl.*, vol. 50, pp. 288–295, Jan. 2014.
- [5] M. Ooshima and C. Takeuchi, "Magnetic suspension performance of a bearingless brushless DC motor for small liquid pumps," *IEEE Trans. Ind. Appl.*, vol. 47, pp. 72–78, Jan. 2011.
- [6] B. Warberger, R. Kaelin, T. Nussbaumer, and J. Kolar, "50-nm/2500-w bearingless motor for high-purity pharmaceutical mixing," *IEEE Trans. Ind. Electron.*, vol. 59, pp. 2236–2247, May 2012.
- [7] D. Steinert, T. Nussbaumer, and J. Kolar, "Slotless bearingless disk drive for high-speed and high-purity applications," *IEEE Trans. Ind. Electron.*, vol. 61, pp. 5974–5986, Nov. 2014.
- [8] H. Mitterhofer, W. Gruber, and W. Amrhein, "On the high speed capacity of bearingless drives," *IEEE Trans. Ind. Electron.*, vol. 61, pp. 3119–3126, June 2014.
- [9] H. Mitterhofer and W. Amrhein, "Motion control strategy and operational behaviour of a high speed bearingless disc drive," in *Proc. IET Power Electron., Mach. Drives Conf.*, pp. 1–6, Mar. 2012.
- [10] D. Steinert, T. Nussbaumer, and J. Kolar, "Topology evaluation of slotless bearingless motors with toroidal windings," in *Power Electronics Conference (IPEC-Hiroshima 2014 - ECCE-ASIA), 2014 International*, pp. 975–981, May 2014.
- [11] C. P. Steinmetz, "On the law of hysteresis," *Encycl. Am. Biogr.*, vol. 9, pp. 3–64, 1892.
- [12] G. Bertotti, A. Boglietti, M. Chiampi, D. Chiarabaglio, F. Fiorillo, and M. Lazzari, "An improved estimation of iron losses in rotating electrical machines," *IEEE Trans. Magn.*, vol. 27, pp. 5007–5009, Nov. 1991.
- [13] Cogent Surahammars Bruk AB, "Typical data for SURA® m270-35a," June 2008.
- [14] S. Iwasaki, R. Deodhar, Y. Liu, A. Pride, Z. Zhu, and J. Bremner, "Influence of PWM on the proximity loss in permanent-magnet brushless AC machines," *IEEE Trans. Ind. Appl.*, vol. 45, pp. 1359–1367, July 2009.
- [15] L. Schwager, A. Tuysuz, C. Zwyssig, and J. Kolar, "Modeling and comparison of machine and converter losses for PWM and PAM in high-speed drives," *IEEE Trans. Ind. Appl.*, vol. 50, pp. 995–1006, Mar. 2014.
- [16] K. Yamazaki and A. Abe, "Loss investigation of interior permanent-magnet motors considering carrier harmonics and magnet eddy currents," *IEEE Trans. Ind. Appl.*, vol. 45, pp. 659–665, Mar. 2009.
- [17] K. Bradley, W. Cao, J. Clare, and P. Wheeler, "Predicting inverter-induced harmonic loss by improved harmonic injection," *IEEE Trans. Power Electron.*, vol. 23, pp. 2619–2624, Sept. 2008.
- [18] A. Borisavljevic, "Electromagnetic modeling of slotless PM machines," in *Limits, Modeling and Design of High-Speed Permanent Magnet Machines*, Springer Theses, pp. 29–70, Springer Berlin Heidelberg, 2013.
- [19] E. Bilgen and R. Boulos, "Functional dependence of torque coefficient of coaxial cylinders on gap width and reynolds numbers," *J. Fluids Eng.*, vol. 95, pp. 122–126, Mar. 1973.
- [20] H. Mitterhofer, D. Andessner, and W. Amrhein, "Analytical and experimental loss examination of a high speed bearingless drive," in *2012 International Symposium on Power Electronics, Electrical Drives, Automation and Motion (SPEEDAM)*, pp. 146–151, June 2012.